

This is the final peer-reviewed accepted manuscript of:

C. Pizzolotto, A. Sbrizzi, A. Adamczak, D. Bakalov, G. Baldazzi, M. Baruzzo, R. Benocci, R. Bertoni, M. Bonesini, H. Cabrera, D. Cirrincione, M. Clemenza, L. Colace, M. Danailov, P. Danev, A. de Bari, C. De Vecchi, M. De Vincenzi, E. Fasci, F. Fuschino, K.S. Gadedjisso-Tossou, L. Gianfrani, K. Ishida, C. Labanti, V. Maggi, R. Mazza, A. Menegolli, E. Mocchiutti, S. Monzani, L. Moretti, G. Morgante, J. Niemela, A. Pullia, R. Ramponi, L.P. Rignanese, M. Rossella, M. Stoilov, L. Stoychev, J.J. Suárez-Vargas, L. Tortora, E. Vallazza, A. Vacchi, *Measurement of the muon transfer rate from muonic hydrogen to oxygen in the range 70-336 K*, Physics Letters A, Volume 403, 2021, 127401.

The final published version is available online at:
<https://doi.org/10.1016/j.physleta.2021.127401>

Rights / License:

The terms and conditions for the reuse of this version of the manuscript are specified in the publishing policy. For all terms of use and more information see the publisher's website.

This item was downloaded from IRIS Università di Bologna (<https://cris.unibo.it/>)

When citing, please refer to the published version.

Measurement of the muon transfer rate from muonic hydrogen to oxygen in the range 70-336 K

C. Pizzolotto^a, A. Sbrizzi^{a,b,*}, A. Adamczak^c, D. Bakalov^d, G. Baldazzi^{e,f},
 M. Baruzzo^{a,g}, R. Benocci^{h,i}, R. Bertoni^h, M. Bonesini^{h,j}, H. Cabrera^{a,s},
 D. Cirrincione^{a,g}, M. Clemenza^{h,j}, L. Colace^{k,l}, M. Danailov^{a,m}, P. Danev^d,
 A. de Bari^{n,o}, C. De Vecchi^o, M. De Vincenzi^{k,p}, E. Fasci^q, F. Fuschino^{e,r},
 K. S. Gadedjisso-Tossou^{a,s,t}, L. Gianfrani^q, K. Ishida^u, C. Labanti^{e,r},
 V. Maggi^{h,i}, R. Mazza^h, A. Menegolli^{n,o}, E. Mocchiutti^a, S. Monzani^{a,g},
 L. Moretti^q, G. Morgante^{e,r}, J. Niemela^s, A. Pullia^{v,w}, R. Ramponi^{v,x},
 L. P. Rignanese^e, M. Rossella^o, M. Stoilov^d, L. Stoychev^{a,1},
 J. J. Suárez-Vargas^a, L. Tortora^k, E. Vallazza^h, A. Vacchi^{a,g,u}

^aSezione INFN di Trieste, via A. Valerio 2, Trieste, Italy

^bDipartimento Politecnico di Ingegneria e Architettura dell'Università di Udine, via delle Scienze 206, Udine, Italy

^cInstitute of Nuclear Physics, Polish Academy of Sciences, Radzikowskiego 152, PL31342 Kraków, Poland

^dInstitute for Nuclear Research and Nuclear Energy, Bulgarian Academy of Sciences, blvd. Tsarigradsko ch. 72, Sofia 1784, Bulgaria

^eSezione INFN di Bologna, viale Berti Pichat 6/2, Bologna, Italy

^fDipartimento di Fisica ed Astronomia, Università di Bologna, via Irnerio 46, Bologna, Italy

^gDipartimento di Scienze Matematiche, Informatiche e Fisiche, Università di Udine, via delle Scienze 206, Udine, Italy

^hSezione INFN di Milano Bicocca, Piazza della Scienza 3, Milano, Italy

ⁱDipartimento di Scienze dell'Ambiente e della Terra, Università di Milano Bicocca, Piazza della Scienza 1, Milano, Italy

^jDipartimento di Fisica G. Occhialini, Università di Milano Bicocca, Piazza della Scienza 3, Milano, Italy

^kSezione INFN di Roma Tre, Via della Vasca Navale 84, Roma, Italy

^lDipartimento di Ingegneria, Università degli Studi Roma Tre, Via V. Volterra 62, Roma, Italy

^mSincrotrone Elettra Trieste, SS14, km 163.5, Basovizza, Italy

ⁿDipartimento di Fisica, Università di Pavia, via A. Bassi 6, Pavia, Italy

^oSezione INFN di Pavia, Via A. Bassi 6, Pavia, Italy

^pDipartimento di Matematica e Fisica, Università di Roma Tre, Via della Vasca Navale 84, Roma, Italy

^qSezione INFN di Napoli e Dipartimento di Matematica e Fisica, Università della Campania "Luigi Vanvitelli", Viale Lincoln 5, Caserta, Italy

^rINAF-OAS Bologna, via P. Gobetti 93/3, Bologna, Italy

^sThe Abdus Salam International Centre for Theoretical Physics, Strada Costiera 11, Trieste, Italy

^tLaboratoire de Physique des Composants à Semi-conducteurs (LPCS), Département de physique, Université de Lomé, Lomé, Togo

^uRiken Nishina Center, RIKEN, 2-1 Hirosawa, Wako, Saitama 351-0198, Japan

^vSezione INFN di Milano, via Celoria 16, Milano, Italy

*Corresponding author

Email address: Antonio.Sbrizzi@cern.ch (A. Sbrizzi)

¹Current address: Institute of Solid State Physics, Bulgarian Academy of Sciences, 72, Tzarigradsko Chaussee, Blvd., 1784 Sofia, Bulgaria

^w*Dipartimento di Fisica, Università degli Studi di Milano, via Celoria 16, Milano, Italy*
^x*INFN-CNR, Dipartimento di Fisica, Politecnico di Milano, piazza Leonardo da Vinci 32,
Milano, Italy*

Abstract

The first measurement of the temperature dependence of the muon transfer rate from muonic hydrogen to oxygen was performed by the FAMU collaboration in 2016. The results provide evidence that the transfer rate rises with the temperature in the range 104-300 K. This paper presents the results of the experiment done in 2018 to extend the measurements towards lower (70 K) and higher (336 K) temperatures. The 2018 results confirm the temperature dependence of Λ_{pO} observed in 2016 and sets firm ground for comparison with the theoretical predictions.

Keywords: X-rays, $LaBr_3(Ce)$, transfer rate, oxygen, muonic atoms, muonic hydrogen, muonic X-rays

1. Introduction

The goal of the FAMU experiment is to extract the Zemach radius of the proton, with an accuracy better than 1%, from a measurement of the hyperfine splitting of muonic hydrogen ground state (ΔE_{hfs})[1].

The experiment consists in counting the number of muon transfers from muonic hydrogen (μp) to oxygen (μO) when a low energy muon beam stops in a hydrogen target containing a fraction of oxygen of the order of 1% (by weight). The target is contained in a high reflectivity optical cavity where an intense laser with finely tunable frequency is injected. After the formation of μp atoms, the muon transfer process leads to the creation of excited μO atoms whose de-excitation cascade gives rise to the K_α , K_β and K_γ spectral lines of muonic oxygen (133 keV, 158 keV and 167 keV) which provide the signature of the muon transfer process. The muon transfer probability is larger when muonic hydrogen has a higher thermal energy, as confirmed by our recent measurement [2]. If the laser is tuned to the right hyperfine splitting transition energy, the μp atoms, predominantly occupying the lower singlet spin state, will be excited to the triplet state. When de-excited in collision with the surrounding H_2 molecules to the singlet state, muonic hydrogen acquires kinetic energy due to the non-radiative de-excitation process, which translates in a larger muon transfer probability. By tuning the laser wavelength on the maximum number of detected X-rays, it is possible to provide a precise measurement of ΔE_{hfs} .

The knowledge of the muon transfer rate from μp to μO (Λ_{pO}) is important to optimize the experimental conditions for the measurement of ΔE_{hfs} [3].

Since 2013, four preliminary measurements without the laser system have been performed in preparation for the spectroscopic data taking. In 2016, the collaboration dedicated an entire data taking session to the measurement of Λ_{pO} as a function of temperature in the range 104-300 K[2]. The same experimental setup was used in March and December 2018 to extend the measurements down to 70 K and up to 336 K. This paper presents the results of the analysis performed to extract the temperature dependence of Λ_{pO} from 2018 data.

2. Experimental setup

The FAMU experiment is performed at the RIKEN-RAL[4] facility which provides a pulsed-muon beam with a repetition rate of 50 Hz. Each bunch consists of two gaussian muon spills (FWHM = 70 ns) separated by about 320 ns. In order to maximize the probability of muonic hydrogen formation in the target, the muon beam momentum was set to 55 MeV/c in the 2018 data taking. The average muon rate at 55 MeV/c is about 3×10^4 /s.

The RIKEN-RAL facility has four muon beam delivery ports. The experiment was installed at Port4 in 2016, while Port1 hosted the experiment in 2018. Compared to Port4, Port1 is better isolated from the external environment and the detectors operate in more stable temperature conditions.

A detailed description of the experimental setup can be found in Ref.[5]. The cryogenic target contains an aluminium cylindrical vessel filled with the mixture of hydrogen and oxygen and it is surrounded by different types of X-ray detectors. The vessel is internally coated with a thin layer of heavy materials (gold and nickel) to stop outgoing muons. The fast nuclear capture of muons in the coating material suppresses the photon background associated to the slow muon capture in the aluminium walls.

The analysis presented in this paper is based on data recorded with six scintillating counters. Each counter consists of a $LaBr_3(Ce)$ cylindrical crystal (1 inch diameter and 1 inch long) coupled to an Hamamatsu R11265U-200 photomultiplier. Waveforms are sampled with a 14-bit 500 Ms/s CAEN V1730C digitizer and recorded in time windows of 8.19 μ s (12-bit TDC).

The rise time of photomultiplier signals (τ_r) is close to the time bin of the digitizer (2 ns). In order to improve signal reconstruction, τ_r is increased with a pulse shaper within the limit of negligible pile-up effects ($\tau_r = 16$ ns). In 2016, τ_r was set to 12 ns.

The trigger provided by the beam facility was adjusted to start data acquisition about 300 ns before the arrival of the first muon spill.

3. Data sample

The temperature dependence of Λ_{pO} is measured by changing the temperature of the cryogenic target system hosting the H_2/O_2 mixture. The gas pressure increases with the temperature because the target is sealed by a valve which keeps a constant gas density inside the target[2]. The transfer rate from μp atoms was measured at each temperature. The analysis presented in this paper is based on data recorded during two runs taken in the same experimental conditions, in March and December 2018.

March 2018 data were taken at four temperatures (272 K, 300 K, 323 K and 336 K). The maximum temperature reachable by the cryogenic target sets the upper limit on the temperature. The cryogenic-cooler helium compressor works up to a pressure of 22.8 bar which corresponds to a temperature of 350 K on the cold head. For safety reasons, the temperature of the cold head was kept below 340 K, the target temperature being slightly lower (336 K) due to heat losses along the copper braids connections between the cold head and the target.

The cooling system of the final spectroscopy experiment will be based instead on liquid nitrogen in order to minimize the vibrations transmitted to the laser system. For this reason, December 2018 was mostly devoted to take data at about the liquid nitrogen temperature (80 K). Data at lower temperatures were taken to explore the region of oxygen condensation. Figure 1 shows the time-dependence of the H_2/O_2 target temperature in the 2018 data taking.

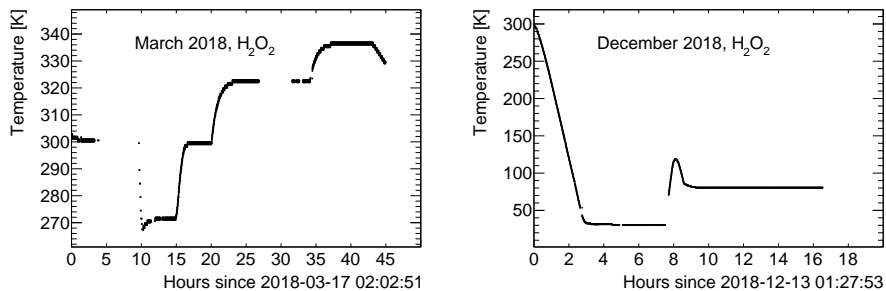


Figure 1: Time-dependence of the H_2/O_2 target temperature in March (left) and December (right) 2018 data taking.

During the first two hours of data taking in December 2018, the target temperature decreased almost linearly from 300 K to 30 K.

Data taken at variable temperature between 100 and 300 K are used to compare the muon transfer rate measured in 2018 to the one measured in 2016 at constant temperature. Even though the two measurements are not performed in the same temperature conditions, the comparison is necessary to extract the oxygen concentration in the 2018 target, as it will be explained in Sec.4.

The March 2018 sample consists of 4.1 M triggers on the H_2/O_2 target and 1.1 M on pure hydrogen for background estimation, while the December 2018 sample has 1.3 M triggers on the H_2/O_2 target and 0.7 M on pure hydrogen.

4. Data analysis

An example of digitized waveform recorded with the FAMU data acquisition system after baseline subtraction is shown in Fig. 2.

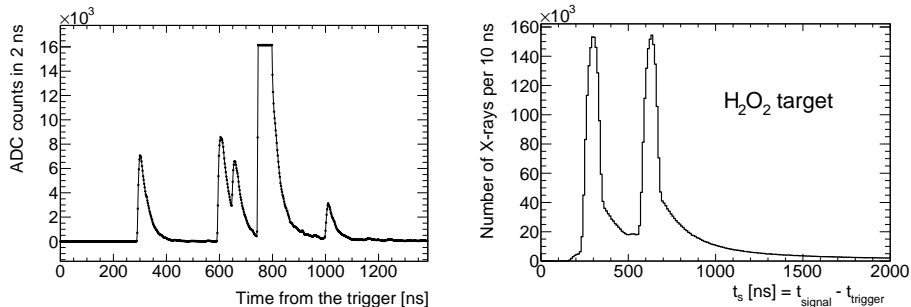


Figure 2: Example of a digitized waveform (left). Each pulse corresponds to an X-ray. The 1st and the 5th pulse are well separated, the 2nd and the 3rd overlap, the 4th pulse saturates the FADC counter. Example of starting time distribution of signals recorded with a $LaBr_3(Ce)$ detector when muons are captured in the H_2/O_2 target (right).

The starting time of a pulse (t_s) is obtained by requiring that the first derivative of the waveform is larger than three times the local average fluctuation above the mean. The baseline RMS is calculated in the proximity of t_s . Pulses with a baseline RMS larger than 20 ADC counts are rejected to improve the energy resolution. The right panel in Fig. 2 shows an example of t_s distribution. The two peaks at 300 ns and 630 ns are the prompt X-ray produced at the arrival of the two muons spills. Delayed X-rays are produced at time larger than the arrival of the second muon spill ($t_s > 900$ ns).

The pulse amplitude is evaluated at the time in which the first derivative of the waveform goes back to zero. If the derivative does not cross the zero, the pulse is tagged as unresolved. Unresolved pulses and pulses lying above unresolved pulses are rejected. In order to suppress pile-up effects that might spoil the energy resolution of the detector, a minimal time separation between pulses is required ($\Delta t_s > 30$ ns). In case of overlapping pulses, the exponential tail of the previous pulse is subtracted. Pulses that saturate the FADC counter (2^{14}) are rejected.

The pulse amplitude is calibrated in energy by using prompt X-rays from elements present in the target, i.e. aluminium (65.8 keV, 88.8 keV, 346 keV), nickel (107 keV, 309 keV). Prompt X-rays are selected in time windows defined around the arrival time of the two muon spills (240-340 ns and 570-670 ns). Delayed X-ray signals from oxygen (133 keV) and photons from electron-positron annihilation (511 keV) are also used for the energy calibration.

Each calibration point is obtained by fitting the pulse-height spectrum with a combination of a gaussian peak and a functional model for the background in the region of a given emission line. The systematic errors are evaluated by changing the background description model and the pulse selection criteria. Figure 3 shows the calibration curve of a $LaBr_3(Ce)$ detector used in this analysis.

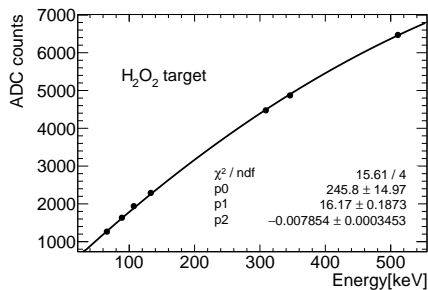


Figure 3: Calibration curve of a $LaBr_3(Ce)$ detector. Vertical error bars are the squared sum of gaussian mean errors and systematic errors on background modelling and pulse selection. The fit to a second degree polynomial function is superimposed. Errors are smaller than the marker size.

Figure 3 shows that the relation between amplitude and energy fits well to a second degree polynomial equation. The energy resolution of the $LaBr_3(Ce)$ detector in Fig. 3 is 10% FWHM at the K_α line of oxygen (133 keV).

4.1. Detector live time and selection efficiency

Detector live time and selection efficiency are calculated with data-driven methods. The duration of saturated pulses is used to estimate the live time. The selection efficiency is the fraction of identified and non-saturated pulses that are resolved and far from other pulses ($\Delta t_s > 30$ ns).

The simulation shows that 99.9% of the pulses are correctly identified by the reconstruction software and that the cut on Δt_s suppresses the systematic effects on pulse amplitude determination. Figure 4 shows the average live time and the selection efficiency of the six available $LaBr_3(Ce)$ detectors as a function of the time after trigger.

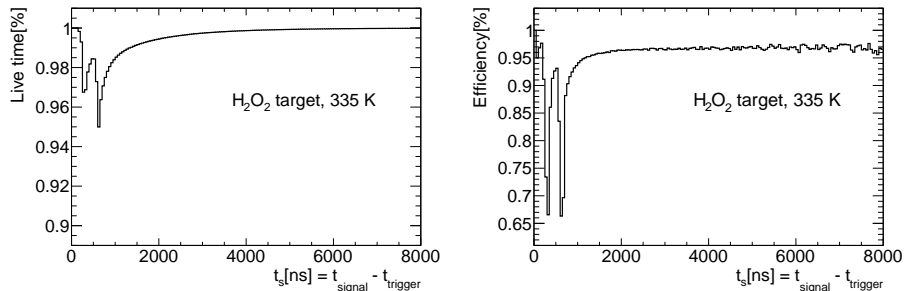


Figure 4: Average live time (left) and selection efficiency (right) at 336 K of the six available $LaBr_3(Ce)$ detectors as a function of the time after trigger in 50 ns time bins.

Live time and selection efficiency are smaller in the proximity of the two muon spills due to a larger pile-up probability. Target gas composition has a negligible effect on live time and selection efficiency.

4.2. X-ray counting

The number of muon transfers to oxygen is measured by counting the number of delayed oxygen X-rays recorded by $LaBr_3(Ce)$ detectors.

Background is evaluated by measuring the number of delayed X-rays produced in the H_2 target. According to the simulation, the main source of background is emission of bremsstrahlung photons by electrons originating from muon decays, while the contribution of prompt X-rays produced in the target material (aluminium, nickel and gold) is not relevant.

Figure 5 shows the energy spectrum of delayed X-rays recorded with all the available $LaBr_3(Ce)$ detectors, before and after background subtraction. The normalization of the background sample is done in an energy range without X-ray lines (250-350 keV).

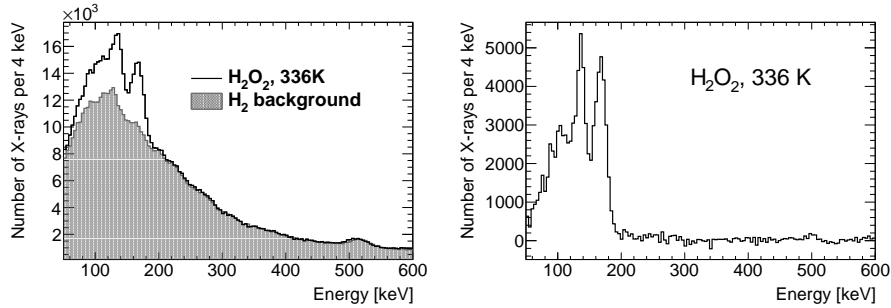


Figure 5: Energy spectra of delayed X-rays produced in H_2/O_2 and H_2 with t_s in the range 900-1200 ns (left). Spectra are normalized in the range 250-350 keV. The temperature of the H_2/O_2 target was 336 K, while pure hydrogen was at 300 K. Background subtracted energy spectrum (right).

The signal spectrum shows the K_α line of oxygen and a second peak corresponding to the unresolved K_β and K_γ lines. The signal region to the left of the K_α oxygen line is populated by X-rays that deposit only a fraction of their energy in the scintillation counter.

Figure 6 shows the number of oxygen X-rays per trigger in December 2018 as a function of the target temperature.

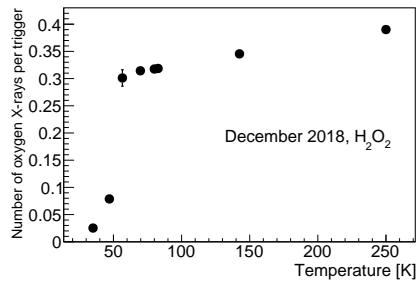


Figure 6: Number of oxygen X-rays per trigger in December 2018 as a function of the target temperature. The temperature of the hydrogen target used to estimate background is 80 K.

Below the temperature of oxygen condensation (60 K) it is not possible to measure the muon transfer rate to oxygen because the signal goes to zero.

4.3. Transfer rate measurement

Λ_{pO} is extracted from the time dependence of the measured number of muon transfers to oxygen in the H_2/O_2 target after the thermalization of μp atoms.

At a given temperature T , the number of μp atoms in the target ($N_{\mu p}$) changes with the time t according to the formula:

$$dN_{\mu p}(t) = -N_{\mu p}(t)\lambda_{dis}(T)dt \quad (1)$$

The total disappearance rate of μp atoms, $\lambda_{dis}(T)$, can be expressed as:

$$\lambda_{dis}(T) = \lambda_0 + \phi[c_p\Lambda_{pp\mu} + c_d\Lambda_{pd}(T) + c_O\Lambda_{pO}(T)] \quad (2)$$

where λ_0 is the disappearance rate of the muons bound to protons, $\Lambda_{pp\mu}$ is the $pp\mu$ formation rate in μp collisions with hydrogen nuclei, Λ_{pd} is the muon transfer rate from μp to deuterium, Λ_{pO} is the muon transfer rate from μp to oxygen atoms, ϕ is the atom density in the gaseous target, c_p , c_d and c_O are the hydrogen, deuterium and oxygen atomic concentrations in the target. The value of the parameters in Eq. 2 and the fitting procedure to extract Λ_{pO} from the time dependent muon transfers to oxygen are reported in Ref.[1]. The only difference is the value of c_O . In March and December 2018, the target was prepared starting from a gas mixture with an initial oxygen weight concentration² of $c_O = 4.6\%$. The gas mixture was diluted with hydrogen to reach the ideal conditions in which $c_O = 0.3\%$ but the procedure was such that the final oxygen concentration in the target exposed to the beam could not be precisely assessed. Therefore, c_O is extracted from data with the procedure reported in Sec. 4.4.

Assuming a given c_O value, Λ_{pO} is extracted from data by counting the number of X-rays in adjacent time bins, starting from 300 ns after the second spill. For each time bin, the integral of the background subtracted energy spectrum in the range 60-190 keV is corrected by live time and selection efficiency.

Figure 7 shows the rate of muon transfers to oxygen measured with all the available $LaBr_3(Ce)$ detectors as a function of the time after trigger at 336 K

²The oxygen concentration c_O is used in units of atomic concentration in the formula of Eq. 2, and in oxygen weight concentration in the rest of the paper.

and 80 K. March 2018 data are divided in 50 ns bins starting from 900 ns. December 2018 data are logarithmically binned from 1000 ns on.

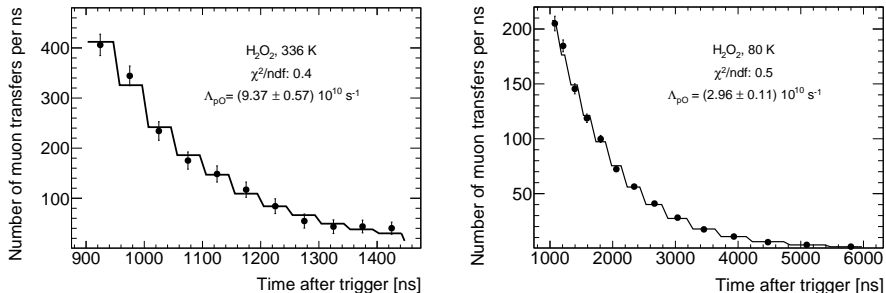


Figure 7: Time dependence of the rate of muon transfers to oxygen measured with all the available $LaBr_3(Ce)$ detectors in March-2018 at 336 K (left) and December-2018 at 80 K (right). The error bars are the sum in quadrature of the statistical and the background-related systematic uncertainties. The fit to extract Λ_{pO} is superimposed.

The measurement of Λ_{pO} is stable against variations of the fitting range towards larger values, which is a proof that prompt X-rays background above 900 ns is negligible.

The statistical uncertainty is calculated assuming a Poissonian distribution of the number of muon transfers. One of the leading sources of systematic uncertainties is background normalization which is evaluated as the maximum variation of the measured number of muon transfers when the subtracted energy spectra undergo a fluctuation of 1σ in opposite directions. Section 4.4 is dedicated to the evaluation of the systematic effect on the target gas composition. Other systematic effects are evaluated in Ref.[1] but they are neglected because their overall contribution is smaller than 1%.

4.4. Data-driven estimate of the oxygen weight concentration

The value of c_O used in Fig. 7 is extracted from data by normalising 2016 and 2018 data taken at the same temperatures.

The first step is fitting the transfer rate measured as a function of temperature in 2016[2] to the lowest order polynomial that well describes the data. The

final choice is a 2^{nd} degree polynomial with coefficients k_{2016} (constant term), k_1 and k_2 (higher order terms).

The second step is to assume an initial c_O value allowing for a first estimate of Λ_{pO} at the normalization temperatures: 272 K and 300 K in March, 104 K, 153 K, 201 K, 240 K, and 272 K in December.

The third step is fitting separately March and December 2018 data to the same 2^{nd} degree polynomial equation, by letting the constant term $k_{2018}(c_O)$ as the only degree of freedom (k_1 and k_2 are fixed). The final value of c_O results from the minimization of the χ^2 defined as:

$$\chi^2(c_O) = \frac{[k_{2018}(c_O) - k_{2016}]^2}{\sigma_{2018}^2 + \sigma_{2016}^2} \quad (3)$$

where the σ is the error on the k parameter.

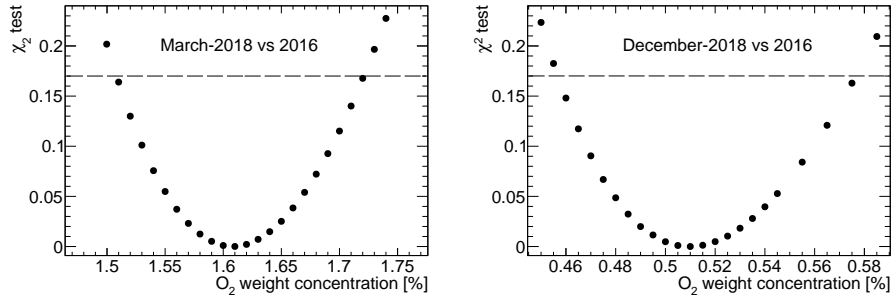


Figure 8: χ^2 of the scaling to 2016 data as a function of the oxygen weight concentration. The horizontal line indicates a χ^2 probability of 68%.

The oxygen weight concentration at the minimum χ^2 is $c_O = 1.61 \pm 0.11\%$ in March 2018 and $c_O = 0.51 \pm 0.06\%$ in December 2018 (see Fig. 8). The quoted error on c_O corresponds to a χ^2 probability of 68%. The total systematic uncertainty on c_O is obtained by adding in quadrature the relative uncertainty provided by the supplier (3%). A similar procedure in which the χ^2 of Eq.3 is calculated by comparing directly 2016 and 2018 data points, without any functional fit, leads to consistent results.

Figure 9 shows the 2^{nd} degree polynomial fit to the 2016 data, together with the 2018 data obtained with c_O at the minimum χ^2 . The December 2018 data

are taken at variable temperatures, while March 2018 and 2016 data are taken at a fixed temperature. The temperature associated to each 2018 data point is the weighted mean calculated in a range where the temperature decreases linearly with time (more details in Sec. 3), the weight being the number of events at a given temperature. The temperature ranges are chosen in a way that the weighted means correspond to the temperatures of 2016 data points.

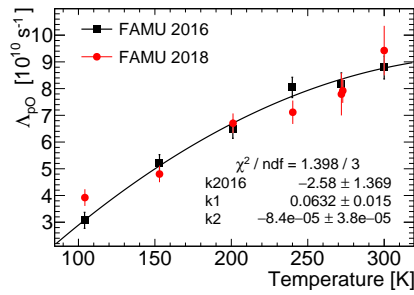


Figure 9: Second degree polynomial fit to the 2016 data [2] used in the procedure to determine the oxygen weight concentration in 2018. Normalised 2018 data are superimposed. The inset shows the reduced χ^2 and the fit parameters, $k1$ and $k2$ being the coefficients of the first and the second degree terms.

5. Results

Table 1 reports the measurements of Λ_{pO} performed at constant temperature, with the exception of the value obtained at 70 K when the temperature was decreasing linearly from 79 K to 60 K (more details in Sec. 3).

$T[\text{K}]$	$\Lambda_{pO}[10^{10}s^{-1}]$	χ^2/ndf
70	* $2.67 \pm 0.40 \pm 0.32$	1.1
80 ± 0.5	$2.96 \pm 0.11 \pm 0.36$	0.5
323 ± 0.5	$8.88 \pm 0.62 \pm 0.66$	0.3
336 ± 0.5	$9.37 \pm 0.57 \pm 0.70$	0.4

Table 1: Measurements of the muon transfer rate to oxygen (Λ_{pO}) at different temperatures. The error on the temperature T indicates the maximum variation of temperature measured with a mK precision during data-taking. The measurement marked by (*) was performed while the temperature was decreasing from 79 to 60 K, 70 K being the event weighted mean. Additional informations can be found in the Supplementary Material. The first error on Λ_{pO} is the sum in quadrature of the statistical uncertainty and the systematic uncertainty associated to background subtraction. The second error is the systematic uncertainty associated to the target gas composition. The last column reports the reduced χ^2 of the fit to extract Λ_{pO} .

Figure 10 shows the results reported in Tab. 1 together with the 2016 measurements [2], previous experimental results [6] and the predictions of two theoretical models by Le and Lin [7] and Dupays [8].

The 2018 results confirm the rise of Λ_{pO} with the temperature observed in 2016 and extends the measurements down to 70 K and up to 336 K.

The available theoretical predictions do not provide an accurate description of the measurements. However, we observe that a multiplicative factor of 2.0 applied to the model of Ref.[7] leads to a good description of the FAMU data, in particular for the points above 100 K where the χ^2/ndf is 0.7.

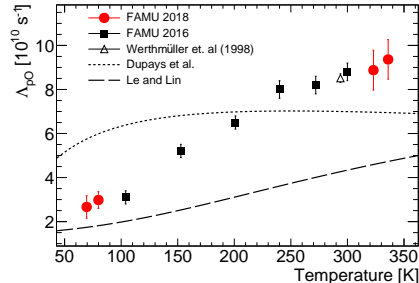


Figure 10: Measurement of Λ_{pO} as a function of the temperature extracted from 2018 data. The vertical error bars includes statistical and total systematic effects. Previous experimental results [2, 6] and theoretical predictions [8, 7] are superimposed.

6. Conclusions

Data taken with the FAMU detector in 2018 have been analysed to extract the temperature dependence of Λ_{pO} in the range 70-336 K. The 2018 measurements have been anchored to the 2016 results in the common temperature ranges by scaling the oxygen concentration of the gas in the target. The 2018 results confirm the temperature dependence of Λ_{pO} observed in 2016 and extends the measurements down to 70 K and up to 336 K. The measurements are in disagreement with the theoretical predictions, as reported already in 2016. Since then, new models have been developed but their predictions are not yet public.

7. Acknowledgements

The research activity presented in this paper has been carried out in the framework of the FAMU experiment funded by Istituto Nazionale di Fisica Nucleare (INFN). We thank RAL and the RIKEN-RAL facility for the support and the help in the set-up of the experiment. We thank the Criotec company for the construction of the FAMU target and for their technical support. D.B., P.D. and M.S. acknowledge the support from Grant DN 08-17 of the Bulgarian Science Fund.

References

- [1] E. Mocchiutti *et al.*, FAMU: study of the energy dependent transfer rate $\Lambda_{\mu p \rightarrow \mu O}$, Journal of Physics: Conference Series 1138 (2018) 012017. doi:10.1088/1742-6596/1138/1/012017.
- [2] E. Mocchiutti *et al.*, First measurement of the temperature dependence of muon transfer rate from muonic hydrogen atoms to oxygen, Phys. Lett. A 384 (126667). doi:10.1016/j.physleta.2020.126667.
- [3] C. Pizzolotto *et al.*, The FAMU experiment: muonic hydrogen high precision spectroscopy studies, Eur. Phys. J. A 56 (2020) 185. doi:10.1140/epja/s10050-020-00195-9.
- [4] T. Matsuzaki *et al.*, The RIKEN-RAL pulsed muon facility, Nucl. Instr. Meth. A 465 (2001) 365. doi:10.1016/S0168-9002(01)00694-5.
- [5] A. Adamczak *et al.*, The FAMU experiment at RIKEN-RAL to study the muon transfer rate from hydrogen to other gases, JINST 13 (2018) P12033. doi:10.1088/1748-0221/13/12/P12033.
- [6] Wertmüller *et al.*, Energy dependence of the charge exchange reaction from muonic hydrogen to oxygen, Hyperfine Interactions 116 (1998) 1–16. doi:10.1023/A:1012618721239.
- [7] A.-T. Le, C. D. Lin, Muon transfer from muonic hydrogen to atomic oxygen and nitrogen, Phys. Rev. A 71 (2005) 022507. doi:10.1103/PhysRevA.71.022507.
- [8] A. Dupays, B. Lepetit, J. A. Beswick, C. Rizzo, D. Bakalov, Nonzero total-angular-momentum three-body dynamics using hyperspherical elliptic coordinates: Application to muon transfer from muonic hydrogen to atomic oxygen and neon, Phys. Rev. A 69 (2004) 062501. doi:10.1103/PhysRevA.69.062501.